Fire spread upslope: Numerical simulation of laboratory experiments

X. Sánchez-Monroy[a],[*], W. Mell[b], J. Torres-Arenas[a], B.W. Butler[c]

[a] *División de Ciencias e Ingenierías, Campus León, Universidad de Guanajuato, Loma del Bosque 103, Lomas del Campestre, 37150, León Guanajuato, Mexico*
[b] *U.S. Forest Service, Pacific Wildland Fire Sciences Lab, 400 N. 34th St., Suite 201, Seattle, WA, 98103, USA*
[c] *U.S. Forest Service, Rocky Mountain Research Station, 5775 Hwy 10 W, Missoula, MT, 59808, USA*

ARTICLE INFO

ABSTRACT

Numerical simulations of laboratory-scale experiments, with no wind imposed, were performed for fuel bed slopes ranging from 0° to 45°. The implementation of a vertical symmetry plane (SP) placed, span-wise, along the middle of the computational domain, was assessed as an approach to reduce computational cost. The simulations were performed with Wildland-urban interface Fire Dynamics Simulator (WFDS). The experimental trends of the compared quantities were reproduced well by the simulations. Radiative heat transfer is the dominant mechanism of heating for slope angles between 0° and 22°, and convection heat transfer mechanism starts to be relevant and becomes more important than radiation for slopes of 31° and 45°. Similar to other studies, it was found a "critical" angle of $\approx 22^{o}$. For slopes angles greater than the critical value, there are significant changes in the wind conditions at the base of the flame which result in a more rapid increase in the rate of spread with increasing slope.

1. Introduction

One of the most critical factors in wildfire propagation is the slope of the terrain, mostly because of its strong influence on the fire front's rate of spread [1–5]. Other important characteristics of fire behavior influenced by slope are the mass loss rate [6], flame residence time [7], and flame tilt angle [8,9], which all increase with the slope. In general, flame geometry is deeply influenced by the slope, playing an important role in the acceleration of the spreading fire and heat transfer [7,9,10]. For instance, an increased flame tilt (due to an increased slope) benefits the heat transfer to the preheated zone in the fuel bed, resulting in a flame front shape changing from U to a V [7,10].

Slope consequences are frequently described in a similar way to those of the wind speed, due to their effect of increasing the extent of the preheating zone ahead of the fire as the flames become closer to the unburned fuel. Combinations of these effects have been extensively considered for different fuels in lab-scale experiments [4,11–13]. However, considering the slope and wind factors separately helps to identify the principal effects of each on flame behavior. Experiments designed to examine the effects of slope without an imposed wind have been conducted [6,7,14–19]. For instance, laboratory experiments to explore the roles of radiation and convection heat transfer for different slopes have been conducted [16] in pine-needle fuel beds. These show a

dominant effect of the radiative heat transfer for a slope angle between 0° and 20°, but when the slope angle increased to 31° convective heat transfer becomes dominant. Similar findings were obtained in field experiments performed by Morandini et al. [15]. More recently, Morandini et al. [18] and Grumstrup [19] investigated the reasons why the role of convective heat transfer increases as the slope increases by focusing on the flow near the flame base and the occurrence of flame attachment.

Physics-based models, of various types, have been applied to explore the influence of wind and topography on fire spread [5,20–22]. Morandini et al. [20] used a non-CFD approach a model based on radiation heat transfer to compare laboratory ROS under various slope and wind conditions, finding a good agreement for slope angles ranging between 0° and 20°. FIRETEC, a CFD physics-based model developed at Los Alamos National Laboratory, has been used to simulate wildfire behavior in inhomogeneous topography and fuels to study the coupled influences of wind and slope [5]. The possibility that slope effects depend on the fuel bed structure have also been analysed using FIRETEC [21].

Physics-based models using the methods of computational fluid dynamics (CFD), like the one implemented here, explicitly model both radiation and convection heat transfer (to some approximation) and can be used to help to improve our understanding of the physical processes

---

driving fire behavior. However, full resolution of the processes occurring over the large range of spatial and temporal scales characterizing fire is not possible with present-day computers. Thus, approximations to the governing equations must be made and special numerical approaches implemented (e.g., large eddy simulation (LES)), whose impact must be characterized to establish acceptable bounds of applicability thorough validation studies.

The current work is a validation study of the Wildland-urban interface Fire Dynamics Simulator (WFDS) [23,24], thorough comparison to laboratory-scale experiments, with no imposed wind. The experiments provide direct measurements of fire spread, mass loss, and flame properties, as a function of fuel bed slope [25]. We examine the capability of WFDS to reproduce the results of such experiments for slope angles from 0° to 45°.

Simulations of this kind, are computationally expensive due to the high spatial ($\approx$ 2 cm) and temporal ($\approx$ 0.001 s) resolution required to numerically solve the governing equations throughout the simulated experimental domain. The simulations performed here required from 56 to 229 processors, depending on the simulation slope case (higher slope cases, which needed a larger computational-domain height, required more processors). Therefore, the use of a vertical symmetry plane (SP) placed, span-wise, along middle of the computational domain (i.e., middle of the fuel bed) was tested as a method to decrease the computational cost. With this assumption, only half of the experimental domain needs to be simulated and the computational cost is reduced by half.

Previous validation studies of the WFDS model have included simulation of laboratory experiments [24,26–29]. Specifically, comparison of WFDS, with a modified approach to handling the process of drying, with piloted ignition of live fuels was performed by Anand et al. [28]. Laboratory experiments in a furniture calorimeter were performed by Perez et al. [29] to compare simulated and measured values of heat release rate from spreading fires in a pine needle bed under no-slope and up-slope conditions. Also, field scale experiments have been simulated [23,30,31]. These include simulations of Australian grass fires [23], fire spread through surface fuels of the Brazilian Amazon [31], and the wind flow within and above forest canopies [30]. It should be noted that the Australian grassland simulations use a different vegetation and thermal degradation model, both better suited to the coarser computational grid necessary for the larger domain, than in the present study at the laboratory scale. Thus, the modeling approach used in the present study would not carry over to outdoor-scale simulations of flames of similar size without prohibitively large computational cost. However, the results of smaller scale studies can be used to support reduced fire-physics models that are not as sensitive to grid resolution constraints (e.g., Mell [32]).

In addition to examining the capability of WFDS to reproduce the experimental results and the SP assessment, in this work we analysed several fire behavior properties in order to explore possible explanations for the slope dependence of fire behavior, and particularly, for the nonlinearity of the rate of spread as a function of slope.

2. Experimental methodology

The slope experiments were conducted at the USFS's Laboratory in Missoula by Butler et al. [25]. Coarse excelsior (shredded aspen, *Populus*

tremuloides) heartwood was selected as fuel. Excelsior was uniform in size (approximately 2.5 × 0.8 mm cross-section) and randomly oriented to form a fuel array with an approximately constant bulk density. The experiments were designed to measure the fire spread rate with fuel bed slopes ranging from −16 to 45°, as measured from the horizontal plane. Three different fuel bed depths, δ, (2.54 cm, 7.62 cm and 15.24 cm) were used with three different packing ratios, β_e, (0.005, 0.01 and 0.03), resulting in nine different experimental tests. The experimental errors could not be characterized here because each experimental case was conducted only once. Fuel moistures ranged from 5 to 8% on a dry mass basis. The platform beneath the excelsior fuel bed was made of 902 Machinable Alumina Silicate and was 1 m wide by 4.6 m long. The fires were ignited by applying electric current to a coiled nichrome wire placed in a 2 cm deep by 1 m wide tray of gasoline/diesel mixture [25].

Light sensors were placed along the edge of the fuel bed every 0.5 m and positioned 25 mm above the fuel bed surface. These were used to measure the arrival and passing time of the flame. When the light sensor trace reaches 0.25 of its peak, the onset of flaming is assumed to occur; and when the output had decayed to 0.15 of the peak, flaming is assumed to have ceased. A mass scale of dimensions 0.25 m × 0.4 m (in the spread and cross spread direction, respectively) was centred under the fuel bed with its closest edge 3 m from the ignition point. It was used to measure the total mass over its surface every 0.2 s.

Fire rate of spread and flame geometry were measured for each experimental test. The rate of spread was measured by dividing the length of the fuel bed by the time the flame front required to move from the ignition location to the opposite end of the fuel bed. In some cases, the rate of spread was also gathered from analysis of video footage. Generally, these two methods agreed within ± 10% [25]. In this work, a methodology for ROS calculation from the data light sensors is also implemented. Fire image analysis was used to compute flame behavior characteristics such as flame depth, flame height and flame angle as a function of the slope for each experiment.

3. WFDS simulations

Computer simulations were conducted for the experimental cases with δ = 7.62 cm and δ = 15.24 cm. The slope values of each case are given in Table 1 with the corresponding values of δ used in the simulation indicated within brackets.

Experimental cases with β_e = 0.005 were not considered in the results of the present work because for all fuel bed depths the fire in the simulation extinguishes after a few seconds for angles less than 31°. This happens because the relatively small amount and loosely packed fuel results in conditions that too marginal to hold the combustion process for the less steep slopes. Conversely, for the steeper slope cases, convective and radiative heat transfer increase enough to support fire propagation. In the experiments, the low amount of fuel, for the β_e = 0.005 cases, produces discontinuities in the fire front; this behavior is indicated with a circle in Fig. 1 for slope angles of 0° and 22°. Likewise, for the cases with δ = 2.54 cm and slopes less than 25°, individual flamelets burning separately along each fuel particle had been observed [25]. These conditions (β_e = 0.005 and δ = 2.54 cm) were on the margin of supporting a continuous flame front. These marginal conditions are outside the modeling approximations used in the derivation of the model equations numerically solved in WFDS which

Table 1
Experimental test scenarios which were simulated. The moisture, on a dry mass basis, is an average of the experimental values for slopes presented in the table.

Test Scenario	Fuel depth, δ (cm)	Packing ratio, β_e	Fuel load, w (kg m^2)	Slope (degrees)	Mean moisture, m (%)
1	7.62 [8]	0.01	0.318	0, 8, 16, 22, 31, 45	7.85
2	7.62 [8]	0.03	0.955	0, 8, 16, 22, 31, 45	8.10
3	15.24 [15,16]	0.01	0.617	0, 8, 16, 22, 31, 45	7.45
4	15.24 [15,16]	0.03	1.850	0, 8, 16, 22, 31, 45	8.17

a)   **b)**

Fig. 1. Experimental fire-front views with β_e = 0.005. (a) Slope angle 0°, δ = 15.24 cm; (b) slope angle 22°, δ = 7.62 cm.

assume that relevant variation in the vegetation, heat flux, and flame are resolved by the computational grid.

3.1. Simulation inputs

For each of the simulated experimental cases given in Table 1, the height of the numerical domain was selected in order to capture the entire simulated flame before and during quasi-steady (if it is reached) fire behavior. This results in a domain height ranging from 1.68 m to 6 m depending on the flame height and slope of the fuel bed.

Heat transfer between the gas phase and the platform supporting the fuel bed and the vertical retaining walls with a thickness of 2 cm are modeled. The material properties of Kaowool insulator are used (see Table 2). Kaowool has similar thermal characteristics to the material used in the substrate and is an approximation for the retaining walls.

The experimental ignition procedure was modeled by using hot particles with a fixed temperature of 800 °C distributed throughout a volume 4 cm × 1 m × δ (spread direction, cross-spread direction, fuel bed depth, respectively). This igniting temperature is reached in 0.5 s and lasts for 5.5 s.

Some of the main thermo-physical properties needed as input parameters for numerical simulation are described below:

1. Fuel bed properties
   (a) Geometry: the fuel bed is represented as a 3D rectangular array of fuel elements. Since the two fuel bed depths, δ = 7.62 cm and δ = 15.24 cm, are not exactly resolved by the grid these are rounded to the closest integer divisible by the grid resolution used (e.g. if the grid resolution is 2 cm, δ = 15.24 cm rounded to 16 cm but if grid resolution is 1 cm, then it's rounded to 15 cm).
   (b) Packing ratio: $\beta_e = \rho_b/\rho_e$ is taken from the experiments, therefore, the bulk density, ρ_b, is chosen to be consistent with β_e and the fuel element density ρ_e.
2. Fuel element properties
   (a) Fuel element density: ρ_e = 398 kg m^{-3} was used, which corresponds to *Populus tremuloides.*
   (b) Moisture content: M is taken from the experimental data of each case and it is based on the dry mass.
   (c) Initial temperature: fuel element initial temperature was assumed to be the same as the reported air temperature of 27 °C.
   (d) Surface-to-volume ratio: σ_e = 3096 m^{-1}.
   (e) Char fraction: the average of the measurements for Douglas fir foliage, stems, and wood as measured by Sussot [33] was used, χ_{char} = 0.26.

Table 2
Fuel bed substrate properties for numerical simulations.

Density	272 kg/m^3
Specific heat	1.1 kJ/kg · K
Emissivity	0.80
Thermal conductivity (temperature dependent)	0.06–0.22 W/m · K

(d) Drag coefficient: $C_{d,e}$ is used for a cylinder in a cross flow (see Eq. (B.16)).
3. Gas phase properties
   (a) Heat of combustion: Δh_c = 17700 kJkg^{-1} is the heat released per kg of gaseous fuel consumed. It was the value reported by Mell et al. [24], as the heat of combustion does not vary enough to be significant in the numerical evaluation of the fire [33].

3.2. Simulation measurments

In order to select a time region to consistently compute and compare flame properties (mainly the geometry of the flame and the ROS), a quasi-steady region of the simulated fire behavior was defined. This region in time is identified when the heat release rate (HRR) curve becomes constant with time. If this state is not reached, then the ROS is computed when the flame front is located at a distance of 1.5 m–3 m from the ignition line.

Table 3 shows the simulation cases where the quasi-steady region is reached ($\sqrt{}$), and those for which the HRR curve did not become constant (×). Unsteady behavior was also observed in the experiments since the ROS for the trailing and leading edges exhibit an accelerated behavior for the steeper slope cases. This means that the portion of fuel bed consumed is not constant in time and neither, therefore, is the HRR.

Rate of spread (ROS) is computed from "devices" in WFDS that mimic the experimental light sensors, placed at 10 cm above the fuel bed retaining wall, every 0.5 m along the edge of the fuel bed. The devices give the incident radiant flux (kW m^{-2}) approximately every 0.2 s, which is averaged in time over 5 time steps. The flame arrival time is identified when the device time trace first reaches half of its peak value. The duration of the flame at a device location is determined by time interval between the arrival time trace and when time trace decays down to half its peak value. These times as a function of the position are used to perform a linear fit to determine the corresponding ROS for each simulation case.

Other fire behavior variables were computed: the flame base (FB), tilt angle (TA), flame depth (FD), flame length (FL) and the angle of separation between the flame and the platform (SA) for the purpose of this work. A schematic representation of these variables and the methodology used to compute them are given in Appendix A.

Table 3
The presence or absence of quasi-steady behavior in each simulation case is denoted by the symbol $\sqrt{}$ and ×, respectively.

Test Scenario	0°	8°	16°	22°	31°	45°
1	–	$\sqrt{}$	$\sqrt{}$	$\sqrt{}$	×	×
2	$\sqrt{}$	$\sqrt{}$	×	×	×	×
3	$\sqrt{}$	$\sqrt{}$	$\sqrt{}$	×	×	×
4	$\sqrt{}$	$\sqrt{}$	×	×	×	×

3.3. Grid resolution and symmetry plane approach

An analysis is performed to evaluate the sensitivity of the simulation results to the grid resolution and the SP approach. In order to determinate the appropriate grid resolution to the parametric tests, the procedure performed by Perez-Ramirez et al. [29] is followed. From this analysis, the grid cell sizes needed to simulate the test scenarios 1 and 3 range from 0.01 m to 0.036 m, and for test scenario 2 and 4 from 0.02 m to 0.037 m. Therefore, computational grid resolutions of 0.01 m and 0.02 m were used to examine the impact on the numerical ROS and the HRR for the 22° slope case of test 1 (see Table 1).

Results showed a minimal effect of grid resolution on the ROS and the HRR, whether the SP is used or not. Thus, the SP offers a very good option to reduce the computation cost, having just a minimal influence on fire behavior because for most of the cases its effect on ROS is the same order in magnitude as the calculation errors and has no dependence on the slope angle of the terrain. Therefore, in order to save computational time, the SP approach and the grid cell size of 2 cm are used for the following results with 22° and the steeper slope cases and 1 cm is used for the smaller slope cases since the lower-slope cases require finer grid resolution to resolve the smaller fire depths. The fuel bed length is 4 m (or 5 m for the 31° and 45° slope cases).

From the production runs, it was found that on the 0° slope case with $\beta_e = 0.01$ and $\delta = 7.62$ cm, the simulated fire extinguishes after 30 s. Several ignition methods where used, with none resulting in fire propagation. Also, another drag model [34] was considered to increase the wind flow, giving the same result of unsuccessful flame propagation. Larger values of the shape factor ($C_{s,e}$ = 3/8 and 1) result in successful fire spread; these results are not reported here because a shape factor of cylinder is used in the present work (i.e., $1/2\pi$), but we consider this an important finding to be shared (see Appendix B.4 for precise definition of $C_{s,e}$). It points to the need for well designed, supporting, measurements to test and develop submodels, such as the model for momentum drag, as was done by El Houssami et al. [35]. Unfortunately, since these experiments were conducted in the past this was not possible. The need for a better drag force model for the fuel geometry used here will be discussed later.

For slopes greater than 0° the WFDS ROS is larger that the measured ROS, and the difference depends on the fuel bed slope angle. For example, the difference is 120% for 8° slope, while for 45° is only 14%. The maximum mass loss rate ($\dot{m}_{max}$) computed from the simulations shows also an overestimation of the experimental results. As a consequence, empirical bounds of the maximum value allowed for the rate that fuel gases can be created per unit of volume in a grid cell were determined and imposed as an input parameter in the simulations. For each simulation test scenario, the bound was computed based on the experimental value for a slope of 31° and applied to slopes ≤ 31°. The use of a local maximum bound on the simulated volumetric mass loss rate, can significantly reduce the ROS, depending on the specific slope case. For a slope of 8°, the ROS decreases 60%, while for 31° only 16%.

A bound on the pyrolysis mass loss rate based on experimental measurements has been implemented before by Overholt et al. [26]. It has also been de facto implemented through the choice of the pyrolysis model itself (Mell et al. [23] and Houssami et al. [36]). The requirement of this bound points to the need for a tightly coupled experimental and simulation effort in which the various component sub models are developed through supportive measurements. This would better determine the empirical parameters in the submodels, such as momentum drag, convective heat transfer, radiative absorption, radiative fraction, and the parameters in Arrhenius kinetics. When this is done, better agreement between model predictions and simulation can occur. An example of a close knit experimental and simulation study is the study of Perez-Ramirez et al. [29] who considered fire spread in a pine needle bed (both level and sloped) under a calorimeter. Unfortunately, the experiments of interest here were conducted many years ago and this information is not available. Even though the use of the experimental bound, does not result in a reproduction of the experimental results with high accuracy, it is important to note that with or without bounds on the mass loss rate, the general trend of the ROS behavior as a function of the slope is captured by the simulations, as will be discussed below.

4. Simulation results and discussion

In this section, the ability of WFDS to reproduce the observed fire behavior will be evaluated through the comparison to several measures of fire behavior. For each case, simulated flame properties were computed at several instants of time. Mean values of these quantities and their corresponding standard deviations are presented. Likewise, an analysis of the physical mechanisms involve in the non-linearity of the ROS, as a function of the slope, is presented.

4.1. Simulation vs experiment

We compared two methods of determining the ROS from experimental observations: the experimental ROS reported by Butler et al. [25] and the ROS compute from the data provided by the light sensor instruments following the same methodology to compute the WFDS ROS from numerical devices. The results of both methods (except for slopes of 45° slope case, since photocell data was not available) are shown in Fig. 2, and compared with the simulated ROS values. For all the cases compared, both methods have the same trend, and for most of cases, the reported experimental ROS are inside the error bars of the ROS from the light sensor method, which corresponds to a linear fit's standard deviation.

The nonlinearity of the ROS as a function of the slope, found in Butler et al. experiments [25] has been reproduced by the WFDS simulation. In general, the simulated ROS is larger than the experimental
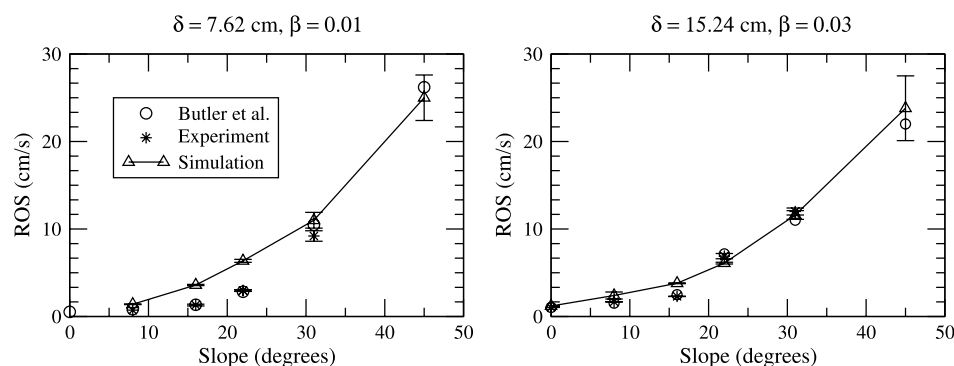

Fig. 2. Rate of spread as a function of the fuel bed slope for the test scenario 1 and 2. The line represents the computed WFDS ROS. Experimental ROS reported by Butler et al. [25] are circles, and ROS derived from the light sensors placed in the experiments are denoted by a star.
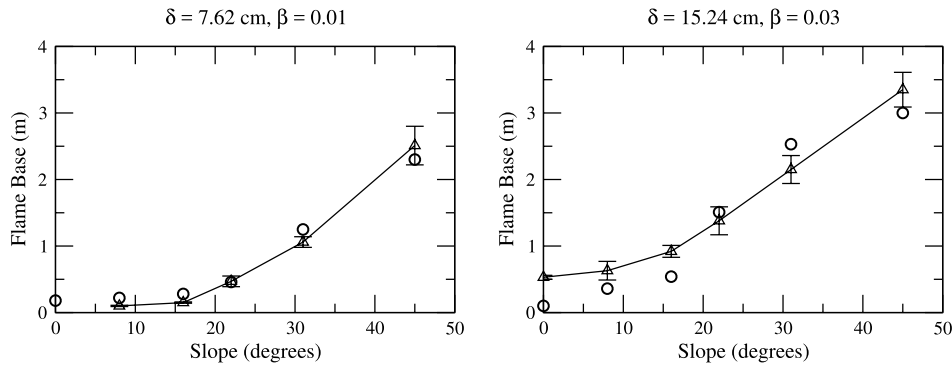
Fig. 3. Flame base (FB in Fig. A.7) as a function of the fuel bed slope for the test scenarios 1 and 4. The circles and triangles indicate the experimental and simulated FB, respectively.

one, and the percentage of overestimation decreases significantly as the slope increases for all the test scenarios. This is consistent with our choice of the mass loss rate bound based on the 31° slope case, as this choice will most likely lead to a bound that is too large for the smaller slopes.

WFDS-based and experimentally observed results of the flame base (FB) and tilt angle (TA) for the test scenarios 1 and 4 are shown in Figs. 3 and 4; the remaining cases are not shown. The observed trend of FB as a function of the fuel bed slope is reproduced by the simulation with better agreement for the lower packing ratio cases. For the steeper slope cases, a better agreement for the FB seems to be obtained. However, for these cases, the flame covers almost the entire fuel bed after a few seconds (in both the simulations and experiments) preventing accurate measures of FB and FD.

Fig. 4 shows that the flame is closer to the unburned vegetation in the simulations than in the experiments. Therefore, there is more likely to be a greater energy exchange from the flame to the fuel bed in the simulated fires, which is consistent with the more rapid ROS obtained in the simulations. The experimentally observed influence of the slope on the flame tilt angle was reproduced in the simulation: the flame inclination toward the unburned fuel increases with the fuel bed slope, from an almost perpendicular position (TA ≈ 20°) to an almost parallel position (AT ≈ 85°) with respect to the fuel bed. This results in an increase of contact area between the flame and the surface; the same behavior has been observed by Silvani et al. [10]. For slope angles between 0° and 22° the tilt angle almost appears to increase linearly with the platform slope; similar to the by Yang et al. [37].

Simulated flame base, flame depth, flame length and tilt angle, were analysed as a function of the slope and amount of fuel. The flame depth and flame base exhibit an evident effect related to the amount of fuel: they cluster according its packing ratio, the cases with the larger packing ratio (i.e., β_e = 0.03) have a larger FD and FB with respect to the cases with β_e = 0.01 (not shown). TA seems to be principally affected by

the slope, exhibiting almost the same behavior regardless of the fuel bed parameters. Fluctuations in flame length increase significantly as the slope increases, therefore, it is not clear if the grouping is also presented in this quantity.

A general overestimation effect is obtained in the simulation results. Without the use of the mass loss rate bound, this overestimation is larger. It is worth noting that WFDS simulations well-predicted ROS and HRR in experiments with a pine needle fuel beds [29] without the use of a mass loss bounds. A potential source of error, in the present simulations, is in the thermal degradation model, which may be better suited for pine needle fuel beds. This points to a recurring observation that rigorous testing and improvement of the sub-models used is needed. Since the overall numerical model is comprised of coupled sub-models, identifying which submodel(s) is the predominant source of the prediction error is a significant challenge and requires repeatable experiments designed to start at a level conducive to testing the sub-models in isolation, in as much as is possible.

During this validation work, a perceptible change of the ROS was observed when the shape factor $C_{s,e}$ in the drag model is modified (see Eq. (B.15)). With the shape factor used here ($1/2\pi$), based on an assumed cylindrically shaped fuel element), the fire extinguished for test scenario 1 and a 0° slope. However, when $C_{s,e}$ is increased, which means that resistance of the vegetative fuel on the fluid flow increases, fire propagation was obtained and the ROS decreased. For example, ROS of $0.85 \, \mathrm{cm \, s^{-1}}$ and $0.57 \, \mathrm{cm \, s^{-1}}$ were computed for a shape factor of 3/8 and 1, respectively. This is for the 0° slope, $\beta = 0.01$, and $\delta = 7.62$ cm case, for which a experimental ROS of $0.53 \, \mathrm{cm \, s^{-1}}$ was measured. Other tests were performed and exhibited a similar behavior.

The drag model employed here extends an empirical drag formula for an isolated cylinder in a crossflow to represent a collection of non-cylindrical solids. It is evident that the elements of the excelsior fuel are not cylinders with the same orientation. We conclude that assuming cylindrical geometry is a coarse model, at least for excelsior, that needs
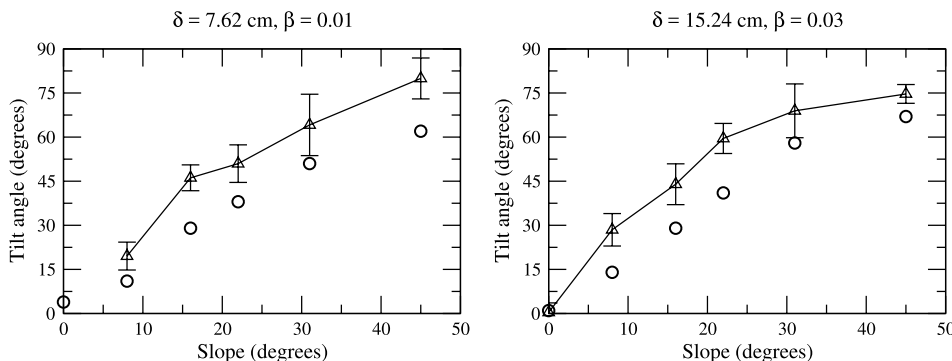

Fig. 4. Tilt angle (TA in Fig. A.7) of the flame as a function of the fuel bed slope for the test scenarios 1 and 4. The circles and triangles indicate the experimental and simulated angles, respectively.

to be improved to reduce the fluid flow through the fuel particles.

Although it is necessary to improve some of the submodels to get a better agreement with the experimental results, it is important to highlight the reliability in the model's ability to reproduce the general trends of the observed fire behavior in these experiments. Such is the case for the nonlinearity of the ROS and the increased contact area between the flame and the surface of the fuel bed as the slope of the fuel bed increases. Therefore, the model can be used to explore physics-based explanations for these results, specifically for the non-linear increase of the ROS with an increase in slope, which is the main finding of the Butler et al. experiments [25].

Another important issue to consider when comparing the simulation and experimental results are the possible systematic errors in the experiment which could not be characterized here because the experimental cases were not repeated.

4.2. Exploring the non-linearity of the rate of spread

In order to explore possible causes of the observed (in the experiments and simulations) nonlinearity of the ROS as the fuel bed slope increased, several simulated variables were analysed such as the heat contribution to the unburned zone, plume attachment, fire fronts and wind flow ahead of the flame front.

To understand the role and relevance of radiative heat flux versus convective heat flux as a function on the slope, the net contribution of the simulated heat fluxes to the unburned vegetative fuel bed are compared at a location at the middle of the top surface of the fuel bed at 2 m from the location of ignition. Simulation results for the divergence of the convective and radiative heat flux (kW m^{-3}), given in Equations B.12 and B.13 (see Appendix B) are analysed for the test scenarios 1 and 4 since they represent the two extreme cases in the simulations concerning to the amount of fuel. Fig. 5 shows instantaneous values of the radiative and convective terms as a function of time for test scenario 1. Two environmental conditions representative of a state of burning are considered and indicated in Fig. 5: a) an approximate ignition time when the average temperature of the vegetation reaches 300 °C (indicates by ×), and b) a post-ignition flaming time when 20% of the dry mass is consumed (indicates by ○). For all the cases, a temperature of

300 °C is reached before 20% of the dry mass is consumed. Similar results are obtained for test scenario 4 (not shown).

For all the analysed fuel bed slope cases, the radiative term prior to ignition is positive. Radiation from the flame heats the vegetation and the magnitude of the radiant heat influx increases as the fire front approaches the measuring point. For slopes between 0° to 31°, the convective term is initially negative (heat loss) or close to zero. Near to the ignition time, the convective term increases in magnitude and becomes positive, especially for slopes greater than 16°. For the 45° slope case, both terms are positive with a similar magnitude. The spatial extent of positive convective heat flux grows with the slope. This is consistent with the increase of the tilt angle and flame length as the slope angle increases. Close to the ignition point, when both heat transfer mechanisms are important, they are of approximately the same magnitude for slope angles between 0° and 22°. However, for 31° and 45°, the convective term is bigger. That is, not only the convection heat transfer mechanism starts to be relevant when the slope angle increases, but it also becomes as, or more, important than radiation. Since the trend of the simulated heat transfer terms with slope is the same in both the test scenarios 1 and 4, these results are independent of the amount of fuel.

In order to analyse the behavior of the hot gases near the unburned vegetative fuel, temperature contours along the x-z plane of symmetry for the gas phase were obtained for different slope cases. It was found that as the slope increases, the hot gases with a temperature around 200 °C extend further along the fuel bed and the plume tilt increases strongly leading to increased flame impingement, with a similar dependence on the slope surface as was shown previously (see Fig. 4). This dependence of the plume attachment length on the inclination angle of the surface has been previously observed in experiments [19,37,38].

A dependence is also found of the fireline shape on the slope angle. For both test scenarios, the fire fronts developed a curvilinear shape during their spread, their shape changes from a relatively flat U, a more pronounced U, to a V as the slope increases (not shown). The same effect is reported in the experiments of Silvani et al. [10], attributed to the presence of fire whirls. In order to determine the existence of whirls in the simulation, more information is needed to compute the vorticity of the wind flux in the flanks of the fire front. This is left as an objective for future work.
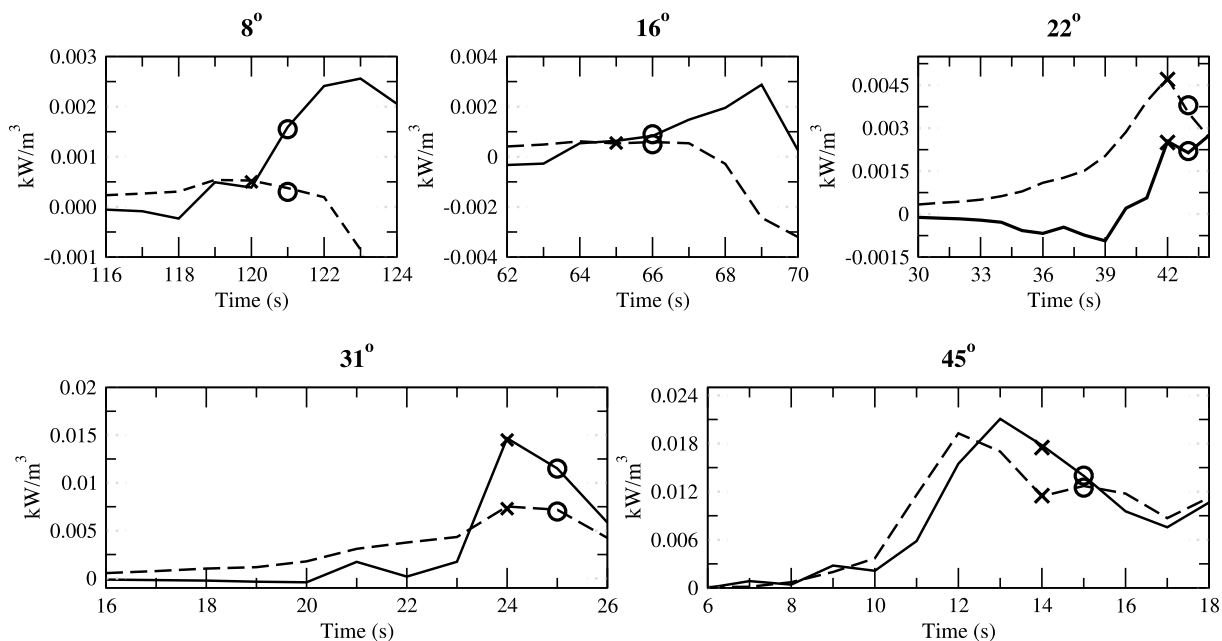

Fig. 5. Time history of the divergence of convective (solid lines) and radiative (dashed lines) heat fluxes for the Test Scenario 1 ($\delta = 7.62$ cm, $\beta_e = 0.01$). The cross (×) indicates the time at which the temperature of the vegetation reaches 300 °C. The circle (○) indicates the time at which 20% of the dry mass is consumed (i.e., post-ignition time).
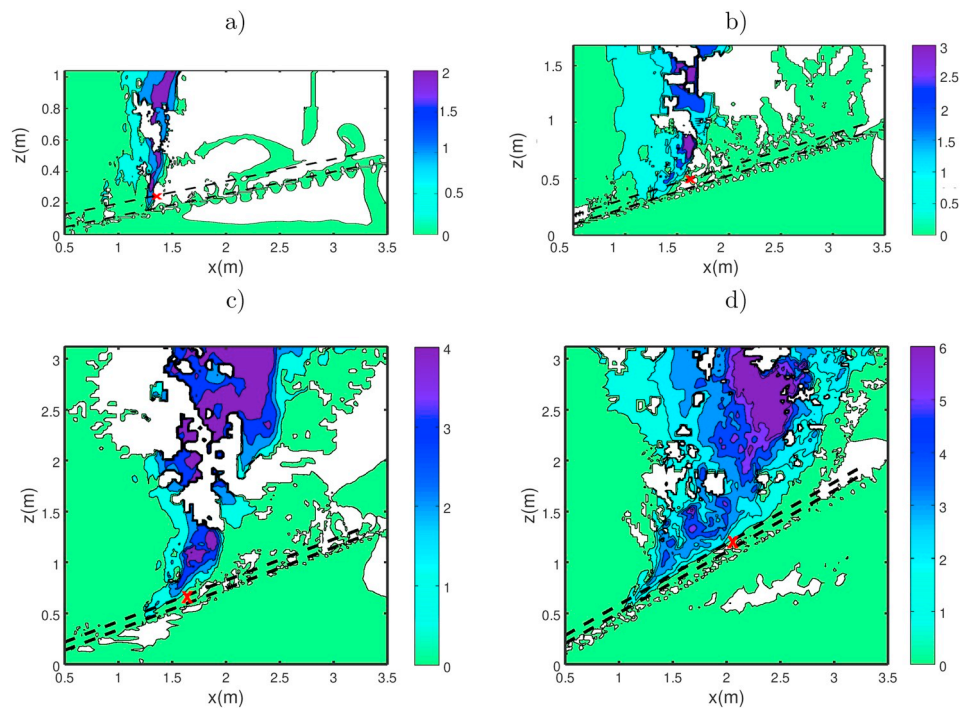
Fig. 6. Color contours (m/s) of the component of the wind parallel to the platform for test scenario 1 fuel bed properties ($\delta = 7.62$ cm, $\beta_e = 0.01$) and slopes of a) 8°, b) 16°, c) 22° and d) 31°. The dashed lines represent the position of the upper and lower boundaries of the fuel bed and the cross symbol is leading edge of the fireline. White regions correspond to wind flow downslope. Green regions correspond to wind flow speed of zero or almost zero, and the region between blue and purple corresponds to wind flow upslope and parallel to the platform. (For interpretation of the references to color in this figure legend, the reader is referred to the Web version of this article.)

So far, similar to other studies, a "critical" angle (which is close to, but larger than, 22°) is observed. For slope angles greater than this critical value, a stronger dependence of fire properties on the slope of the fuel bed exists. However, the existence of this critical angle or the reason why the flame tilt angle increases until reaching an almost parallel position with respect to the fuel bed, or why convective heat transfer becomes more important than radiation heat transfer, is still unclear. This could be attributed to a significant change in the wind flow at the base of the fire. For this reason, wind flow entrained laterally into the fire is analysed.

Wind velocity contours for the test scenario 1 are presented in Fig. 6; here only the component of the wind velocity parallel to the platform is shown for slope angles 8°, 16°, 22°, and 31°. The red symbol × is the leading edge of the fireline. White regions correspond to wind flow downslope and parallel to the platform. Green regions correspond to wind flow speed of zero or almost zero (e.g., less than 0.5 m/s for the slope cases of 8° and 16°), and the region between blue and purple corresponds to wind flow upslope and parallel to the platform. As is shown in the colorbar legends, the maximum value of the wind component parallel to the platform increases with the surface inclination. The region of downslope flow, ahead of the flame front and close to the platform, becomes smaller as the slope increases and is nonexistent for the steepest slope case shown (31°). This transition in wind flow behavior occurs at a slope angle that is consistent with other fire behavior changes discussed above. At a slope between 22° and 31° the downslope flow parallel to the platform and at the base of the flame ceases to exist and wind flow is solely upslope. This will lead to a net positive convective heat flux upslope of the fire base. Similar behavior has been observed in lab-scale experiments across a bed of excelsior by Morandini et al. [14,18], where a increase of air entrainment on the burned side of the flame (left side in Fig. 6) and an inversion of the direction of the local wind ahead of the flame front for surface inclination of 22° was observed.

From these results, we can conclude that the degree to which a

plume tilts over the surface is related to flow parallel to the fuel bed toward the base of the flame. The larger the downhill entrainment flow is, the lower tilt of the flame. Similar discussions regarding flow near the flame base and flame tilt behavior have been presented Grumstrup et al. [19], as a competition between buoyancy force parallel to the platform and the downhill entrainment wind flow.

5. Summary and conclusions

The present work contributes to the validation of WFDS through comparison with fire spread upslope experiments. As we have shown, although a general overestimation in the simulated fire behavior is observed, the model was capable of reproducing the observed trends of a variety of fire behaviors. However, some questions remain open and left for future work. First, the general overestimation of the fire behavior measures in the simulations indicates a potential source of error in the thermal degradation and drag models whose effect can be significant, at least in this kind of vegetative fuel. This points to a recurring observation that rigorous testing and improvement of the sub-models used is needed. This requires repeatable experiments designed to test, in as much as is possible, the submodels in isolation (e.g., momentum drag). Examples of such studies include El Houssami et al. [35] and Ramirez-Perez [29]. On the other hand, the current model could be used for further investigation into the observed trends. This includes the physical mechanisms (e.g., vorticity) involved in fire front shape change from a relatively flat U, to a more pronounced U, to a V as the slope increases. Likewise, it was found that SP approximation is a good approach to simulate this kind of scenarios saving half of the computational cost.

Our analysis showed, similar to other studies, the existence of a "critical" angle where a stronger dependence of fire properties on the slope of the fuel bed is shown. For instance: 1) convective heat transfer becomes as, or more, important than radiation, 2) the longitudinal section of hot gases touching the fuel bed increases dramatically, and 3)

the fire front shape changes from curvilinear U to V shape.

Finally, upslope and downslope wind flow parallel to the platform and near the fuel bed were analysed from the simulation results. Ahead of the flame front, flow downhill toward the flame-base weakens as the slope increases and is replaced by a region with no wind. Thus, larger downhill entrainment flow is associated with lower flame tilt. The onset of an upslope wind through the flame base increases the positive convective heat flux to the upslope fuel bed. These observations contribute to an explanation of the physical mechanism driving the slope

dependence of the flame tilt angle and the nonlinear dependence of the ROS on slope angle.

Appendix A. Simulated measurements

Selected fire behavior variables were computed and compared with the experimental ones: ROS, the flame base (FB), and tilt angle (TA). Additional geometry properties of the flame are computed from the simulation in order to analyse the general behavior of WFDS as a function of the packing ratio and the depth of the fuel bed: flame depth (FD), flame length (FL) and the angle of separation between the flame and the platform (SA). Figure A.7 shows a schematic of the flame indicating each one of these quantities. The methodology used to compute these properties in the simulations is given below.
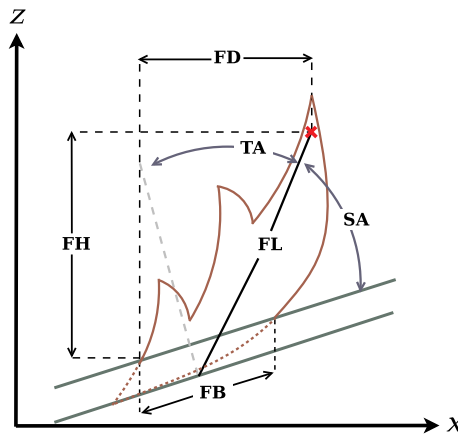

Figure A.7. Diagram from a side view of the simulated flame properties computed. Flame depth (FD), flame base (FB), flame length (FL), tilt angle (TA) and separation angle (SA) are indicated in the flame diagram.

Flame base (FB) Flame base is computed as the average distance between the vegetative fuel particles in ignition or close to ignition (i.e., at $300\,°C \pm 10\,°C$) at the leading edge of the flame and the vegetative fuel particles in char-oxidation (i.e, at $1000\,°C \pm 10\,°C$) at the trailing edge of the flame.

Flame height (FH) Flame height is computed from the local heat release rate per unit volume (HRRPUV) [39]. The height at which approximately 99% of the heat release occurred is obtained and the vertical distance (on the z axis) between this point and the lowest point of the FB is defined as the flame height (see Figure A.7).

Flame length (FL) To compute the flame length, a calibration procedure using the zero slope cases was performed. It was assumed that for zero slope case the tilt angle must be zero wherewith a condition over the HRRPUV at the highest point of the FH is obtained to find the peak of the flame (indicated with a symbol × in Figure A.7). A value of $160\,kW/m^3 \pm 10\,kW/m^3$ in the peak of the flame is obtained as a condition, such that FL is defined as the distance from this point to the middle of the FB.

Flame depth (FD) This property is computed as the horizontal distance (on x axis) from the peak of the flame to the beginning of the FB.

Flame angle Two angles are obtained to characterize the flame behavior. The first one is the tilt angle (TA), the angle between the perpendicular line to the platform and the FL line. The second one is the separation angle (SA) between the FL line and the platform.

Appendix B. Overview of the numerical model

The Wildland-urban interface Fire Dynamics Simulator (WFDS) [23,24] is the computational model used in this work. WFDS is a comprehensive physics-based model in which all the recognized coupled physical processes driving wildland fire behavior are explicitly modeled. This includes convective and radiative heat transfer, gas phase combustion, buoyancy induced flow, and the thermal degradation (drying, pyrolysis, char oxidation) of vegetation. Details of the modeling approach have been provided by Mell et al. [24]. The WFDS model, developed by the U.S. Forest Service and the National Institute of Standards and Technology (NIST), is an extension of the capabilities of the FDS (Fire Dynamics Simulator beta version 6.0), a structure fire behavior model developed by NIST.

Computational fluid dynamics (CFD) methods are used to solve numerically the three-dimensional (or two-dimensional) time-dependent equations governing fluid motion, turbulent combustion, and heat transfer. A large-eddy simulation (LES) approach is used in the numerical model to solve the governing equations for momentum, mass and energy in the gas phase.

A multiphase formulation to account for the exchange of mass, energy, and momentum between the gas phase and solid vegetation is used. The vegetation is assumed to be composed of fixed, thermally-thin fuel elements, approximated as point sources of mass, drag, heat release, and radiative absorption and emission.

A three stage thermal degradation model, coupled to the gas phases, is solved to obtain the temperature of the vegetation: endothermic drying,

endothermic pyrolysis, and exothermic char oxidation. An Arrhenius temperature dependent model is used to obtain the mass exchanges, due to drying, pyrolysis and char oxidation.

Cylindrical vegetative fuel particles were assumed to compute the bulk drag force in the momentum conservation equation due to vegetation. Convective heat transfer assumed forced convection for cylinders in a crossflow using a Reynolds number dependent correlation due to Hilpert [40].

A single, 1-step chemical reaction is used to model the combustion of gaseous fuel generated from the pyrolysis of vegetation [24].

Appendix B.1 Governing equations and modeling approach for gas phase

The implementation of the LES approach for solving the equations for the gas phase is based on a spatial low-pass spatial filter on the instantaneous conservation equations. This low-pass filtering approach implies that turbulent motions larger than a filter width are directly resolved, while those smaller (i.e., subgrid) are modeled using a turbulence closure scheme [24,41].

The filter applied in the LES for an arbitrary scalar ψ can be either implicit to obtain $\bar{\psi}$ or explicit to obtain $\langle\psi\rangle$. Conventional LES quantities are implicitly filtered in the simulation, where the grid is assumed to be the LES low-pass filter. Explicit filtering uses an anisotropic box filter to determine the bulk source terms due to the presence of subgrid fuel elements. Mell et al. [24] provides further details. For completeness, an overview of the governing equations and the numerical approach is given here. The notation below uses the subscript b to denote bulk quantities that are resolved on a computational grid cell of volume V_b. For example, the bulk mass per volume of dry vegetation, resolved on the computational grid, is denoted by $\rho_{b,dry} = \langle m'''_b \rangle_{V_b}$ (kg m^{-3}). In order to handle flows with density fluctuations, a mass-weighted Favre filter is used, such that the Favre filter of the quantity ψ is given by $\tilde{\psi} = \overline{\rho\psi}/\bar{\rho}$. The filtered transport equations for mass, species, momentum, and enthalpy, combined with the equation of state are shown below ($\dot{\psi}$ denotes $\partial\psi/\partial t$).

$$\frac{\partial \bar{\rho}}{\partial t} + \nabla\cdot(\bar{\rho}\tilde{\mathbf{u}}) = \langle \dot{m}'''_b \rangle_{V_b} \tag{B.1}$$

$$\frac{\partial \bar{\rho}\tilde{Y}_i}{\partial t} + \nabla\cdot(\bar{\rho}\tilde{Y}_i\tilde{\mathbf{u}}) = -\nabla\cdot(\bar{\mathbf{J}}_i + \mathbf{J}_i^{sgs}) + \overline{\dot{m}}''' + \langle \dot{m}'''_{b,i} \rangle_{V_b} \tag{B.2}$$

$$\frac{\partial \bar{\rho}\tilde{\mathbf{u}}}{\partial t} + \nabla\cdot(\bar{\rho}\tilde{\mathbf{u}}\tilde{\mathbf{u}}) = -\nabla\bar{p} - \nabla\cdot(\bar{\tau} + \tau^{sgs}) + \bar{\rho}\mathbf{g} + \langle \mathbf{f}''_D \rangle_{V_b} \tag{B.3}$$

$$\frac{\partial \bar{\rho}\tilde{h}}{\partial t} + \nabla\cdot(\bar{\rho}\tilde{h}\tilde{\mathbf{u}}) = \frac{\tilde{D}p_0}{\tilde{D}t} - \nabla\cdot(\bar{\mathbf{q}} + \mathbf{q}^{sgs}) - \nabla\cdot\bar{\mathbf{q}}_r + \langle \dot{q}'''_{c,b} \rangle_{V_b} + \langle \dot{\mathbf{h}}'''_b \rangle_{V_b} \tag{B.4}$$

$$\bar{\rho} = \frac{p_0 \bar{W}}{\mathscr{R}\tilde{T}} \tag{B.5}$$

Flux and source terms are given below in Tables B.4 and B.5.

Table B.4
Constitutive relations and subgrid models.

Species Flux	$\bar{J}_i + \overline{J_i^{sgs}} = -\bar{\rho}\left(\bar{D}_i + \frac{v_t}{Sc_t}\right)\nabla\tilde{Y}_i$
Momentum Flux	$\bar{\tau} = -2\bar{\mu}\left(\tilde{S} - \frac{1}{3}(\nabla\cdot\tilde{u})\mathbf{I}\right)$
	$\tau^{sgs,d} \equiv \tau^{sgs} - \frac{1}{3}\text{trace}(\tau^{sgs})I = -2\bar{\rho}v_t\left(\tilde{S} - \frac{1}{3}(\nabla\cdot\tilde{u})I\right)$
Heat Flux	$\tilde{q} + q^{sgs} = -\left(\bar{k} + \bar{\rho}\tilde{c}_p\frac{v_t}{Pr_t}\right)\nabla\tilde{T} - \sum_i \bar{\rho}\left(\bar{D}_i + \frac{v_t}{Pr_t}\right)\tilde{h}_i\nabla\tilde{Y}_i$

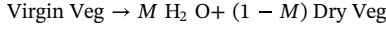#### Table B.5
Summary of source terms.

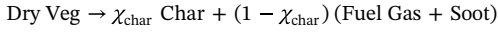| Water vapor	$\langle \dot{m}''_{b,H_2O} \rangle_{V_b} = \beta_e \dot{m}'''_{H_2O,e}$
Fuel vapor	$\langle \dot{m}''_{b,F} \rangle_{V_b} = \beta_e \dot{m}'''_{F,e}$
Fuel (chemical)	$\overline{\dot{m}}'''_F = -\frac{min(\bar{\rho}\tilde{Y}_F, \bar{\rho}\tilde{Y}_{O_2}r_{O_2})}{\tau}, \tau = C_{EDC}\frac{\Delta^2 Sc_t}{v_t}, C_{EDC} = 0.1$
Drag	$<\mathbf{f}''_D>_{V_b} = \beta_e \sigma_e \frac{1}{(2\pi)}C_{D,e}\bar{\rho}|\mathbf{u}_e - \tilde{\mathbf{u}}|(\mathbf{u}_e - \tilde{\mathbf{u}})$
Heat release	$\dot{Q}'''_C = -\overline{\dot{m}}'''_F \Delta\tilde{h}_C$
Radiation	$\nabla\cdot\bar{\mathbf{q}}_r = \kappa[4\pi I_b(\tilde{T} - \tilde{U})] + \langle \nabla\cdot\mathbf{q}_{r,b} \rangle_{V_b}$
	$\langle \nabla\cdot\mathbf{q}_{r,b} \rangle_{V_b} = \kappa_{b,e}[4\pi I_b(T_e) - \tilde{U}]$
	$\kappa I_b(\tilde{T}) = max(\chi_r \dot{Q}'''_C, \kappa\sigma_B \tilde{T}^4/\pi)$
Heat transfer	$\langle \dot{q}'''_{c,b} \rangle_{V_b} = \beta_e \sigma_e h_{c,e}(T_e - \tilde{T})$
Enthalpy	$\langle \dot{h}'''_b \rangle_{V_b} = \sum_i h_i(T_e)\langle \dot{m}'''_{b,i} \rangle_{V_b}$

Appendix B.2 Solid-phase thermal degradation model

The thermal degradation model used here, for thermally thin vegetative fuel, has been employed previously in WFDS [29] and is similar to approaches used by others [36,42,43]. There are three components to the modeled thermal degradation:
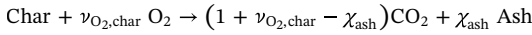
1. Endothermic drying

Virgin Veg $\rightarrow M$ H_2O + $(1 - M)$ Dry Veg

2. Endothermic pyrolysis

Dry Veg $\rightarrow \chi_{\text{char}}$ Char + $(1 - \chi_{\text{char}})$ (Fuel Gas + Soot)

3. Exothermic char oxidation

Char + $\nu_{O_2,\text{char}}$ O_2 $\rightarrow$ $(1 + \nu_{O_2,\text{char}} - \chi_{\text{ash}})CO_2 + \chi_{\text{ash}}$ Ash

here, M is the fuel (i.e., vegetation) moisture mass fraction on a dry weight basis; χ_{char} is the mass fraction of dry fuel that is converted to char during pyrolysis; $\nu_{O_2,\text{char}}$ = 1.65 [42]; χ_{ash} is the mass fraction of char that is converted to ash during char oxidation.

The equation governing the temperature of a thermally-thin fuel element, e, is

$$\rho_e c_{p,e} \frac{dT_e}{dt} = -\Delta h_{\text{vap}} R_{H_2O,e} - \Delta h_{\text{pyr}} R_{\text{pyr},e} - \alpha_{\text{char}} \Delta h_{\text{char}} R_{\text{char},e} - \nabla \cdot \mathbf{q}_{c,e} - \nabla \cdot \mathbf{q}_{r,e}. \tag{B.6}$$

The terms to the right account for, respectively, the endothermic generation of water vapor, endothermic pyrolysis which creates fuel vapor and char, exothermic char oxidation, heat transfer due to conduction between the solid and gas phases, and net heat transfer due to thermal radiation. The fraction of heat released to the solid phase from char oxidation is given by the parameter α_{char}. For this work, α_{char} = 0.5 which as been used by others authors [29,42]. The remaining energy is released in the gas phase. The mass generation terms, R, are described in the next section where Eq. (B.6) is developed in the context of a LES multiphase approach.

Appendix B.3 Multiphase formulation

In general, vegetation is represented as $k = 1, ..N$ different thermally-thin vegetation types. Fuel elements for each type have the same geometrical and thermochemical properties and a temperature equation (Eq. (B.6)) is solved for each vegetation type. Since, for the experiments simulated here, there is only one type of vegetation, excelsior, subscript k takes on a single value (e.g., $k = e$) and is, for simplicity of notation, not used in most of the formulas that follow (e.g., the bulk density of vegetation type k, $\rho_{b,k}$, is denoted ρ_b). The multiphase formulation presented here follows that of Grishin [44] and Larini et al. [45] and is described more fully, in the context of LES, in Mell et al. [24]. Applying the LES explicit filter to Eq. (B.6) results in Ref. [24]:

$$\rho_b c_{p,b} \frac{dT_e}{dt} = -\Delta h_{\text{vap}} R_{H_2O} - \Delta h_{\text{pyr}} R_{\text{pyr}} - \alpha_{\text{char}} \Delta h_{\text{char}} R_{\text{char}} - \langle \dot{q}'''_{c,b} \rangle_{V_b} - \langle \nabla \cdot \mathbf{q}_{r,b} \rangle_{V_b}. \tag{B.7}$$

The bulk density and specific heat for the solid phase take into account components of dry virgin vegetation, moisture, char, and ash:

$$\rho_b = \rho_{b,\text{dry}} + \rho_{b,H_2O} + \rho_{b,\text{char}} + \rho_{b,\text{ash}}, \tag{B.8}$$

$$c_{p,b} = \frac{\rho_{b,\text{dry}} c_{p,\text{dry}} + \rho_{b,H_2O} c_{p,H_2O} + \rho_{b,\text{char}} c_{p,\text{char}} + \rho_{b,\text{ash}} c_{p,\text{ash}}}{\rho_b} \tag{B.9}$$

where c_{p,H_2O} = 4.22 kJ kg^{-1} K^{-1} [40] and $c_{p,\text{ash}}$ = 0.8 kJ kg^{-1} K^{-1} [44]. The specific heat for the dry virgin vegetation [46] and char [47] are temperature dependent:

$$c_{p,\text{dry}} = 0.01 + 0.0037 T_e, \tag{B.10}$$

$$c_{p,\text{char}} = 0.47 + 0.00209 T_k + 0.00685 T_e^2. \tag{B.11}$$

Applying the explicit filter to the terms for mass generation due to drying, pyrolysis and char oxidation modeled via an Arrhenius type kinetics gives the following equations:

$$R_{H_2O} = \rho_{b,H_2O} A_{H_2O} T_e^{-\frac{1}{2}} \exp\left(-\frac{E_{H_2O}}{\mathscr{R} T_e}\right)$$

$$R_{\text{pyr}} = \rho_{b,\text{dry}} A_{\text{pyr}} \exp\left(-\frac{E_{\text{pyr}}}{\mathscr{R} T_e}\right)$$

$$R_{\text{char}} = \rho_g A_{\text{char}} \exp\left(-\frac{E_{\text{char}}}{\mathscr{R} T_e}\right) \frac{\rho_g Y_{O_2} \sigma_e \beta_e (1 + \beta_{\text{char}} \sqrt{\text{Re}_e})}{\nu_{O_2,\text{char}}}$$

where $\beta_e = \rho_b/\rho_e$ is the packing ratio of the bulk vegetation and σ_e is the surface-to-volume ratio of the fuel element. The values of the kinetic constants used here are given in Table B.6. The fuel element based Reynolds number is $\text{Re}_e = \rho_g D_e/\mu$ with $D_e = 4/\sigma_e$ for a cylinder. The Re_e term is included to account for the oxygen blowing effects on char oxidation and the constant β_{char} is equal to 0.2 by default, which is the value used by

Porterie et al. [42]. A modification of WFDS model has been done in which also bound water components are considered and modeled via Arrhenius rate equations, hence, a tree stage decomposition process, consisting of evaporation of bound and free water, pyrolysis, and char oxidation is consider as the solid fuel degradation process [28].

Table B.6
Parameters for solid phase model

Constant	Default Value	Comment
Δh_{vap} (kJ kg^{-1})	2259	[42]
A_{H_2O} ($\sqrt{K}s^{-1}$)	600,000	[42]
E_{H_2O}/R (K)	5800	[42]
Δh_{pyr} (kJ kg^{-1})	418	[42]
A_{pyr} (s^{-1})	36,300	[42]
E_{pyr}/R (K)	7250	[42]
Δh_{char} (kJ kg^{-1})	$-32,740$	[48]
A_{char} (m s^{-1})	430	
E_{char}/R (K)	9000	[42]
α_{char} (−)	0.5	[29,42]
β_{char} (−)	0.2	[42]
$\nu_{O_2,char}$	1.65	[42]

The net divergence of the conductive and radiative heat fluxes are the final two terms in Eq. (B.7). The conductive heat flux makes use of convective heat transfer correlations and is given by.

$$\langle \dot{q}'''_{c,e} \rangle_{V_b} = \sigma_e \, \beta_e \, h_{c,e} (T_e - T_g), \tag{B.12}$$

where $h_{c,e}$ is the convective coefficient from the forced convection over cylinders in cross-flow [40] given in Eq. (B.17).

The radiative transfer term for the solid fuel is written as

$$\langle \nabla \cdot \mathbf{q}'''_{r,e} \rangle_{V_b} = \kappa_e (4\sigma T_e^4 - U), \tag{B.13}$$

where $\kappa_e = \sigma_e \beta_e / 4$ is the absorption coefficient, U is the total irradiance, and σ is the Stefan-Boltzman constant.

Appendix B.4 Drag and convective heat transfer models

The contribution of the drag force on the flow from the subgrid particles within the computational volume is

$$\langle \mathbf{f}''_D \rangle_{V_b} = \frac{1}{V_b} \sum_{k \in V_b} \frac{1}{2} C_{d,k} A_k \bar{\rho} |\mathbf{u}_k - \tilde{\mathbf{u}}|(\mathbf{u}_k - \tilde{\mathbf{u}}). \tag{B.14}$$

Assuming vegetative fuel particles of identical geometry in V_b, the equation above becomes

$$\langle \mathbf{f}''_D \rangle_{V_b} = C_{s,e} \sigma_e \, \beta_e \, C_{d,e} \bar{\rho} |\mathbf{u}_e - \tilde{\mathbf{u}}|(\mathbf{u}_e - \tilde{\mathbf{u}}), \tag{B.15}$$

where $C_{d,e}$ is the drag coefficient, $C_{s,e} = A_e/(2V_e)$, A_e is the cross-sectional area of the fuel element facing the flow, and V_e is the volume of the fuel element. Both $C_{d,e}$ and $C_{s,e}$ depend on the shape of the fuel element. For cylinders, as assumed here, $C_{s,e} = 1/(2\pi)$. The value of the drag coefficient depends on the local Reynolds number as [24,49]:

$$C_{d,e} = \begin{cases} \frac{10}{Re_e^{0.8}}, & Re_e \leq 1, \\ \frac{10(0.6 + 0.4Re_e^{0.8})}{Re}, & 1 < Re_e < 1000, \\ 1, & 1000 \leq Re_e. \end{cases} \tag{B.16}$$

The correlation for the convective heat transfer coefficient is from Hilpert's (which can be found in Incropera and DeWitt [40] is
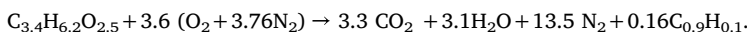
$$h_{c,e} = \frac{k_g Nu}{D_e} = \frac{k_g \sigma_e}{4} C Re_e^m Pr^{1/3}, \tag{B.17}$$

where the coefficients C and m are based on the particle Reynolds number:

$$C, m = \begin{cases} 0.909, \, 0.330, & Re_e \leq 4, \\ 0.911, \, 0.385, & 4 < Re_e \leq 40 \\ 0.683, \, 0.466, & 40 < Re_e. \end{cases} \tag{B.18}$$

Appendix B.5 Gas phase chemical reactions

The combustion of the gaseous fuel is modeled with the simplified stoichiometric relation [46]

$$C_{3.4}H_{6.2}O_{2.5} + 3.6 \, (O_2 + 3.76N_2) \rightarrow 3.3 \, CO_2 + 3.1H_2O + 13.5 \, N_2 + 0.16C_{0.9}H_{0.1}.$$

The molar heat of combustion for a given chemical reaction at constant pressure is [50,51].

$$\Delta H_c \equiv -\sum_i \nu_i H_i(T) = \sum_i \nu_i h_i(T) W_i, \tag{B.19}$$

where ν_i is the stoichiometric coefficient of gas species i. In terms of the fuel mass consumption rate

$$\dot{m}'''_i = r_i \dot{m}'''_F = \frac{\nu_i W_i}{\nu_F W_F} \dot{m}'''_F, \tag{B.20}$$

where $\nu = -1$, $\nu_{O_2} = -3.7$, $\nu_{CO_2} = 3.4$, and $\nu_{H_2O} = 3.1$. Using this, the heat release rate per unit of volume of the combustion process can be represented in terms of the heat of combustion, as

$$\dot{Q}'''_c = -\sum_i \tilde{h}_i \overline{\dot{m}'''_i} = \frac{\overline{\dot{m}'''_F}}{\nu_F W_F} \Delta H_c. \tag{B.21}$$

The filtered chemical source term $\overline{\dot{m}'''_F}$ is obtained from the Eddy Dissipation Concept (EDC) of Magnussen [52], see Table B.5.

Appendix B.6 Thermal radiation transport

Fires from vegetative fuels are heavily soot laden. Since the radiation spectrum of soot is continuous, it is assumed that the gas behaves as a spectrally independent or gray medium. This results in a significant reduction in computational expense. The vegetative fuel is assumed to be comprised of fixed, uniformly distributed (within the bulk volume V_b), non-scattering, perfectly absorbing, subgrid fuel elements.

Following Consalvi et al. [53], for simplicity the fuel element is assumed to be spherical. The absorption coefficient is [54],

$$\kappa_{b,e} = \frac{1}{4} \frac{\rho_{bv,e}}{\rho_e} \sigma_e = \frac{1}{4} \beta_e \sigma_e \tag{B.22}$$

This expression for the absorption coefficient has been used in other fire spread models [23,55–59] and has been experimentally validated for vegetative fuels [60]. The final form of the radiation transfer equation (RTE) is then given by

$$\hat{s} \cdot \nabla \bar{I}(\mathbf{x}, \hat{s}) = \kappa [I_b(\tilde{T}) - \bar{I}(\mathbf{x}, \hat{s})] + \kappa_{b,e} [I_b(T_e) - \bar{I}(\mathbf{x}, \hat{s})]. \tag{B.23}$$

A table containing the values of κ as a function of species mass fractions and temperature for a given mixture of participating gaseous species (H_2O, CO_2) and soot particulate is computed using RadCal [61] before the simulation begins. A soot evolution model is not used. Instead, the mass of soot generated locally is an assumed fraction, χ_s, of the mass of fuel gas consumed by the combustion process. In the WFDS simulations reported here, $\chi_s = 0.02$ is used. Values of χ_s for Douglas fir range from less than 0.01 to 0.025 under flaming conditions [62].

Integrating the RTE (B.23) over all solid angles gives the equation for conservation of radiant energy,

$$\nabla \cdot \bar{\mathbf{q}}_r(\mathbf{x}) = \kappa [4\pi I_b(\tilde{T}) - \bar{U}(\mathbf{x})] + \kappa_{b,e} [4\pi I_b(T_e) - \bar{U}(\mathbf{x})]$$
$$= \kappa [4\pi I_b(\tilde{T}) - \bar{U}(\mathbf{x})] + \langle \nabla \cdot \mathbf{q}_{r,b} \rangle_{V_b}. \tag{B.24}$$

where $\bar{U}$ is the integrated radiation intensity. Equation (B.24) is required in the enthalpy transport equation (B.5) and in the divergence constraint on the velocity divergence derived by taking the material derivative of the equation of state (see Mell et al. [24]).

Capturing the effects of subgrid heterogeneity of the flame temperature requires special treatment of the radiation emission term κI_b since this term depends on the fourth power of the local temperature. In regions where the local mean temperature is lower and spatial gradients of scalars are sufficiently resolved, capturing the effects of the subgrid temperature distribution is less critical. For this reason, we model the gas phase emission term as

$$\kappa I_b(\tilde{T}) = \max(\chi_r \dot{Q}'''_c, \ \kappa \sigma_{0B} \tilde{T}^4 / \pi), \tag{B.25}$$

where χ_r is the fraction of the chemical heat release rate per unit volume that is radiated to the local volume surrounding the flame region. Note that some of this radiation will be absorbed by the surrounding soot and vegetative fuel. As a result, for sufficiently smoke laden fires the fraction of chemical heat release radiated to a location outside the smoke plume will be smaller than the local value. For hydrocarbon pool fires the local value is is $\chi_r \cong 0.30$ to 0.35 while the global value is less, 0.10 [63]. In wood cribs $\chi_r \cong 0.20$ to 0.40 [64]. The value used in the simulations presented here is $\chi_r = 0.35$.

A finite volume method based on that of Raithby and Chui [65] is used to solve the gray gas form of (B.23). It requires approximately 20% of the total CPU time. The spatial discretization of the radiation transport equation is the same as that used in the other gas phase conservation equations. Measured values of the radiative flux in the vicinity of a burning Douglas fir tree were compared to simulated values in Mell et al. [24] and agreed reasonably well. In addition, a large number of validation and verification tests have been conducted to test the radiation solver and the overall FDS modeling system into which WFDS is integrated. The interested reader can find the FDS validation and verification guides through an internet search on the keywords: FDS manuals.

References

[1] W.L. Fons, Analysis of fire spread in light forest fuels, J. Agric. Res. 72 (3) (1946) 93–121.

[2] G.M. Byram, Combustion of Forest Fuels, McGraw-Hill Book Company, New York, 1959.

[3] D.R. Weise, Modelling Wind and Slope-Induced Wildland Fire Behavior, Ph.D. thesis University of California, 1993.

[4] D.X. Viegas, Slope and wind effects on fire propagation, Int. J. Wildland Fire 13 (2) (2004) 143–156.

[5] W.S.S. Linn, Judith Winterkamp Rodman, Carleton Edminster, J Colman Jonah, Coupled influences of topography and wind on wildland fire behaviour, Int. J. Wildland Fire 16 (2007) 183–195.

[6] J.-l. Dupuy, Slope and fuel load effects on fire behaviour: laboratory experiments in pine needles fuel beds, Int. J. Wildland Fire 5 (3) (1995) 153–164.

[7] D.A. Portier, J.A. Valette, The Effects of Slope and Fuel Bed Width on Laboratory Fire Behaviour, (2011).

[8] D.R. Weise, G.S. Biging, Effects of wind velocity and slope on flame properties, Can. J. For. Res. 26 (1996) 1849–1858.

[9] M.A. Finney, S.S. Mcallister, A review of fire interactions and mass fires, J. Comb. 2011 (2011) 14.

[10] X. Silvani, F. Morandini, J.-l. Dupuy, Effects of slope on fire spread observed through video images and multiple-point thermal measurements, Exp. Therm. Fluid Sci. 41 (2012) 99–111.

[11] D.R. Weise, G.S. Biging, Effects of wind velocity and slope on fire behavior, Proc. fifth Int. Symp. (1994) 1041–1051.

[12] R Weise David, S Bining Gregory, Effects of wind velocity and slope on flame properties, Can. J. For. Res. 26 (1996) 1849–1858.

[13] J. Mendes-Lopes, J. Ventura, J.M.P. Amaral, Flame characteristics, temperature–-time curves, and rate of spread in fires propagating in a bed of Pinus pinaster needles, Int. J. Wildland Fire 12 (2003) 67–84.

[14] F. Morandini, X. Silvani, J.-l. Dupuy, A. Susset, Fire spread across a sloping fuel bed: flame dynamics and heat transfers, Combust. Flame 190 (2018) 158–170.

[15] X. Silvani, Experimental investigation of the physical mechanisms governing the spread of wildfires, Int. J. Heat Mass Transf. 19 (5) (2010) 570–582.

[16] J.M. Dupuy, J.L, Slope effect on laboratory fire spread: contribution of radiation and convection to fuel bed preheating, Int. J. Wildland Fire 20 (2011) 289–307.

[17] N. Liu, J. Wu, H. Chen, L. Zhang, Z. Deng, K. Satoh, D.X. Viegas, J.R. Raposo, Upslope spread of a linear flame front over a pine needle fuel bed : the role of convection cooling, Proc. Combust. Inst. 35 (3) (2014) 2691–2698.

[18] F. Morandini, X. Silvani, D. Honoré, G. Boutin, A. Susset, R. Vernet, Slope effects on the fluid dynamics of a fire spreading across a fuel bed: PIV measurements and OH chemiluminescence imaging, Exp. Fluid 55 (8) (2014).

[19] T.P. Grumstrup, S.S. Mcallister, M.A. Finney, M. Fire, U.S.F. Service, Qualitative flow visualization of flame attachment on slopes, Presented at the 10th U. S. National Combustion Meeting Organized by the Eastern States Section of the Combustion Institute; April 23-26, The Combustion Institute, College Park, MD. Pittsburgh, PA, 2017, p. 6.

[20] F. Morandini, P. Santoni, J. Balbi, The contribution of radiant heat transfer to la-boratory-scale fire spread under the influences of wind and slope, Fire Saf. J. 36 (6) (2001) 519–543.

[21] C.E. Rodman R Linn, L Winterkamp Judith, R Weise David, A numerical study of slope and fuel structure effects on coupled wildfire behaviour, Int. J. Wildland Fire 19 (2010) 179–201.

[22] F.A. Pimont, J.A. Dupuy, R.R.B. Linn, Coupled slope and wind effects on fire spread with influences of fire size : a numerical study using FIRETEC, Int. J. Wildland Fire 21 (7) (2012) 828–842.

[23] W. Mell, M.A. Jenkins, J. Gould, P. Cheney, A physics-based approach to modelling grassland fires, Int. J. Wildland Fire 16 (1) (2007) 1–22.

[24] W. Mell, A. Maranghides, R. McDermott, S.L. Manzello, Numerical simulation and experiments of burning douglas fir trees, Combust. Flame 156 (10) (2009) 2023–2041.

[25] B.W. Butler, W.R. Anderson, E.A. Catchpole, Influence of Slope on Fire Spread Rate, USDA For. Serv. Proc, 2007, pp. 75–82.

[26] K.J. Overholt, A.J. Kurzawski, J. Cabrera, M. Koopersmith, O.A. Ezekoye, Fire be-havior and heat fluxes for lab-scale burning of little bluestem grass, Fire Saf. J. 67 (2014) 70–81.

[27] Drew Clayton Castle, Numerical Modeling if Laboratory-Scae Surface-To-Crown Fire Transition, San Diego State University, 2015 Ph.D. thesis.

[28] C. Anand, S. Mcallister, B. Shotorban, S. Mahalingam, D.R. Weise, Physics-based modeling of live wildland fuel ignition experiments in the forced ignition and flame spread test apparatus, Combust. Sci. Technol. 189 (9) (2017) 1–9.

[29] Y. Perez-Ramirez, W.E. Mell, P.A. Santoni, J.B. Tramoni, F. Bosseur, Examination of wfds in modeling spreading fires in a furniture calorimeter, Fire Technol. 53 (5) (2017) 1795–1832.

[30] E. Mueller, W. Mell, A. Simeoni, Large eddy simulation of forest canopy flow for wildland fire modeling, Can. J. For. Res. 44 (2014) 1534–1544.

[31] P. Bufacchi, G.C. Krieger, W. Mell, E. Alvarado, J.C. Santos, J.A. Carvalho, Numerical simulation of surface forest fire in Brazilian Amazon, Fire Saf. J. 79 (2016) 44–56.

[32] W. Mell, The state of physics-based fire modeling and an example of a reduced fire-phisics model, 8th Int. Conf. for. Fire Res. Novemb. 12-16, 2018 Present. FiM_67.

[33] A. Susott, Characterization of the thermal properties of forest fuels by combustible gas analysis + char, For. Sci. 28 (2) (1982) 404–420.

[34] J. Finnigan, Tutbulence in plant canopies, Annu. Rev. Fluid Mech. 32 (2000) 519–571.

[35] M. El Houssami, A. Lamorlette, D. Morvan, R.M. Hadden, A. Simeoni, Framework for submodel improvement in wildfire modeling, Combust. Flame 190 (2018) 12–24.

[36] M.E. Houssami, J. Thomas, A. Lamorlette, D. Morvan, M. Chaos, R. Hadden, A. Simeoni, Experimental and numerical studies characterizing the burning dy-namics of wildland fuels, Combust. Flame 168 (2016) 113–126.

[37] Z. Yang, H.-x. Chen, Experimental study on flame geometry along the inclined surface with and without sidewalls by using a gas burner, Procedia Eng 211 (2018) 925–933.

[38] Y. Wu, H.J. Xing, G. Atkinson, Interaction of fire plume with inclined surface, Fire Saf. J. 35 (4) (2000) 391–403.

[39] T. Ma, J. Quintiere, Numerical simulation of axi-symmetric fire plumes: accuracy and limitations, Fire Saf. J. 38 (5) (2003) 467–492.

[40] D.P. Incropera, F, P, Dewitt, Fundamentals of Heat and Mass Transfer, WILEY, 2007.

[41] S.B. Pope, Turbulent Flows, Cambridge University Press, 2001.

[42] J. Porterie, J.L. Consalvi, A. Kaiss, Loraud, Predicting wildland fire behavior and emissions using a fine-scale physical model, Numer. Heat Tran. 47 (6) (2005) 571–591.

[43] D. Morvan, J.L. Dupuy, Modeling of fire spread through a forest fuel bed using a multiphase formulation, Combust. Flame 127 (1–2) (2001) 1981–1994.

[44] A.M. Grishin, Mathematical Modeling of Forest Fires and New Methods of Fighting Them, Publishing House of the Tomsk University., Tomsk, 1992.

[45] M. Larini, F. Giroud, B. Porterie, J.C. Loraud, A multiphase formulation for fire propagation in heterogeneous combustible media, Int. J. Heat Mass Transf. 41 (6–7) (1998) 881–897.

[46] S. Ritchie, K. Steckler, A. Hamins, T. Cleary, J. Yang, T. Kashiwagi, The effect of sample size on the heat release rate of charring materials, Proc. 5th Int. Symp. (1997) 177–188.

[47] M.G. Grønli, M.C. Melaaen, Mathematical model for wood pyrolysis comparison of experimental measurements with model predictions, Energy Fuels 14 (4) (2000) 791–800.

[48] S. Dahale, Ambarish, Selina Ferguson, Babak Shotorban, Mahalingam, Effects of distribution of bulk density and moisture content on shrub fires, Int. J. Wildland Fire 22 (5) (2013) 625–641.

[49] B. Porterie, D. Morvan, M. Larini, J.C. Loraud, Wildfire propagation: a two-di-mensional multiphase approach, Combust. Explos. Shock Waves 34 (2) (1998) 139–150.

[50] N. Peters, Turbulent Combustion, Cambridge university press, 2000.

[51] T. Poinsot, D. Veynante, Theoretical and Numerical Combustion, RT Edwards, Inc., 2005.

[52] B.F.M.H, B. Hjertager, On mathematical modeling of turbulent combustion with special emphasis on soot formation and combustion, Symp. Combust. 16 (1) (1977) 719–729.

[53] J. Consalvi, B. Porterie, J. Loraud, A formal averaging procedure for radiation heat transfer in particulate media, Int. J. Heat Mass Transf. 45 (13) (2002) 2755–2768.

[54] NAS, A Study of Fire Problems, National Academy of Sciences vol. 949, National Research Council, Washington, DC, 1961 Chapter Append. IV Note Radiat. Transp. Probl. Aris. fire spread, Publ.

[55] D. Morvan, J. Dupuy, Modeling the propagation of a wildfire through a medi-terranean shrub using a multiphase formulation, Combust. Flame 138 (3) (2004) 199–210.

[56] F.A. Albini, A model for fire spread in wildland fuels by-radiation, Combust. Sci. Technol. 42 (5–6) (1985) 229–258.

[57] F.A. Albini, Wildland fire spread by radiation-a model including fuel cooling by natural convection, Combust. Sci. Technol. 45 (1–2) (1986) 101–113.

[58] Y. De Mestre, E. Catchpole, D. Anderson, R. Rothermel, Uniform propagation of a planar fire front without wind, Combust. Sci. Technol. 65 (4–6) (1989) 231–244.

[59] D. Morvan, J. Dupuy, Modeling of fire spread through a forest fuel bed using a multiphase formulation, Combust. Flame 127 (1–2) (2001) 1981–1994.

[60] B. Butler, In Proceedings: 12 Th Conference of Fire and Forest Meteorology, 1993, p. 26.

[61] W. Grosshandler, RadCal: A Narrow Band Model for Radiation Calculations in a Combustion Environment, NIST Tech. Note 1402, Natl. Inst. Stand. Technol., Gaithersburg, MD, 1993.

[62] C. Bankston, B. Zinn, R. Browner, E. Powell, Aspects of the mechanisms of smoke generation by burning materials, Combust. Flame 41 (1981) 273–292.

[63] H. Koseki, G. Mulholland, The effect of diameter on the burning of crude oil pool fires, Fire Technol. 27 (1) (1991) 54–65.

[64] J.G. Quintiere, Principles of Fire Behavior, CRC Press, 2016.

[65] G. Raithby, E. Chui, A finite-volume method for predicting a radiant heat transfer in enclosures with participating media, J. Heat Transf. 112 (2) (1990) 415–423.